

# Effects of Ligand Chemistry on Ion Transport in 2D Hybrid Organic-Inorganic Perovskites

Grace Wei, Alan B. Kaplan, Hang Zhang, Yueh-Lin Loo, and Michael A. Webb\*

2D hybrid organic-inorganic perovskites are potentially promising materials as passivation layers that can enhance the efficiency and stability of perovskite photovoltaics. The ability to suppress ion transport is proposed as a stabilization mechanism, yet an effective characterization of relevant modes of halide diffusion in 2D perovskites is nascent. In light of this knowledge gap, molecular dynamics simulations with enhanced sampling and experimental validation to systematically characterize how ligand chemistry in seven (R-NH<sub>3</sub>)<sub>2</sub>PbI<sub>4</sub> systems impacts halide diffusion, particularly in the out-of-plane direction is combined. It is found that increasing stiffness and length of ligands generally inhibits ion transport, while increasing ligand polarization generally enhances it. Structural and energetic analyses of the migration pathways provide quantitative explanations for these trends, which reflect aspects of the disorder of the organic layer. Overall, this mechanistic analysis greatly enhances the current understanding of halide migration in 2D hybrid organic-inorganic perovskites and yields insights that can inform the design of future passivation materials.

1. Introduction

The hybrid organic–inorganic perovskites (HOIPs) are promising materials for photovoltaic applications due to their bandgap tunability, large absorption coefficients, and long charge-carrier lifetimes, leading to solar cells with high power conversion efficiency and potentially low production cost. [1–4] Rapid

G. Wei, Y.-L. Loo, M. A. Webb Department of Chemical and Biological Engineering Princeton University Princeton, NJ 08544, USA E-mail: mawebb@princeton.edu A. B. Kaplan

Department of Electrical and Computer Engineering Princeton University Princeton, NJ 08544, USA

H. Zhang Department of Chemistry Princeton University Princeton, NJ 08544, USA

The ORCID identification number(s) for the author(s) of this article can be found under https://doi.org/10.1002/aenm.202401087

© 2024 The Author(s). Advanced Energy Materials published by Wiley-VCH GmbH. This is an open access article under the terms of the Creative Commons Attribution-NonCommercial License, which permits use, distribution and reproduction in any medium, provided the original work is properly cited and is not used for commercial purposes.

DOI: 10.1002/aenm.202401087

developments in this technology, most prominently using 3D perovskites with methylammonium (MA) or formamidinium (FA) lead iodide, have remarkably improved power conversion efficiency in recent years, exceeding those of all thinfilm technologies except more costly III-V cells.<sup>[5]</sup> However, the commercialization of perovskite solar cells (PSCs) based on hybrid organic-inorganic perovskites has been limited due to poor operational lifetimes, which stem from the sensitivity of perovskites toward moisture, oxygen, light, and heat.[6-8] Therefore, understanding the mechanisms of degradation in perovskites and formulating effective mitigation strategies<sup>[9]</sup> are of significant interest to enhance the viability and reliability of perovskites for everyday usage.

Mobile ionic defects along the interfaces and interior of perovskite films are key intrinsic sources of instability

in HOIPs.[10] Accumulation of these defects at transport layer interfaces not only increases charge-carrier recombination, thereby reducing cell efficiency but can also lead to permanent device degradation due to undesirable chemical reactions with adjacent solar cell layers.[11-13] Therefore, using passivation layers to reduce film defects is a promising approach to improve PSC efficiency and stability.[14-18] Low-dimensional perovskites (2D or 1D) can be created by replacing the MA or FA cation with bulkier organic cations, yielding structures with alternating inorganic and organic layers.[19-22] Recent experiments demonstrate that such low-dimensional perovskites can function as effective passivating materials that inhibit ionic transport with appropriately chosen ligand chemistry.[23,24] However, while numerous substituent effects on various metrics have been reported,[25,26] it remains unclear how to rationally and effectively tailor ligand chemistry for this purpose.

The scarcity of mechanistic investigations into ion transport in low-dimensional HOIPs is a key factor contributing to the existing knowledge gap. While multiple studies, both experimental and theoretical, have been conducted on ion transport in 3D MAPbI<sub>3</sub>, [27–31] research on 2D HOIP systems is primarily limited to butylammonium lead iodide (BAPI), [32] limiting insights into ligand effects. Moreover, in contrast to 3D HOIP systems, transport in 2D HOIPs may be anisotropic relative to the plane formed by the inorganic cation layers. For example, in-plane thermal conductivity has been found to be a factor of 1.5 times larger than out-of-plane thermal conductivity in BAPI. [33] However, to



www.advancedsciencenews.com

MATERIALS www.advenergymat.de

what extent halide diffusion differs in-plane versus out-of-plane is unknown. Experimentally, in-plane activation energies for ion diffusion have been measured in BAPI, phenylethylammonium lead iodide (PEAPI), and quasi-2D HOIPs, [23,24,32] vet out-of-plane measurements are lacking. Computationally, technical limitations emerge. Common static electronic structure calculations do not address finite-temperature dynamical properties.[34-38] Meanwhile, ab initio molecular dynamics (MD) simulations have explored conformational dynamics of small organic cations[39] and electron-hole recombination<sup>[40]</sup> but fall short in characterizing halide diffusion. For this, classical simulation is better suited, and recent development of the classical MYP force field<sup>[41]</sup> has facilitated MD of in-plane ion transport in BAPI and quasi-2D HOIPs. [42,43] Nevertheless, implications for passivation [44] will require characterization of out-of-plane diffusion, which is complicated by the traversal of the organic layer and a correspondingly complex free energy landscape.[31,45,46]

In this work, we systematically investigate the impact of ligand chemistry on vacancy-assisted ion transport in 2D HOIPs. Our analysis focuses on out-of-plane halide diffusion, which relates to transport from one site on the lattice to a vacancy located across a layer of organic ligands, to generate insights related to passivation based on mitigation of ion transport. Using MD simulations in tandem with enhanced sampling, we characterize the free energy landscape for out-of-plane halide diffusion in 2D HOIPs for different ligands and identify significant correlations between ligand chemistry and transport behavior. We demonstrate the impact of structural and chemical ligand properties like flexibility and electronegativity on halide diffusion and discuss the parameters for designing an optimal organic layer for mitigating ion diffusion in 2D HOIPs. These insights can inform the development of effective 2D HOIP passivation materials for stable and efficient PSCs.

## 2. Overview of Systems

To study how organic ligand chemistry affects halide diffusion, we explore a series of model 2D HOIP systems that systematically differ in ligand chemistry in several ways (Figure 1). The prototype Ruddlesden-Popper (RP) phase 2D HOIP has the layered structure shown in Figure 1a that alternates between octahedra formed by an inorganic cation and a halide anion and organic ligands. This structure can be described by the formula (R-NH<sub>3</sub>)<sub>2</sub>BX<sub>4</sub>, where 'B' is an inorganic cation with + 2 formal charge, 'X' is a halide anion (formal charge of-1), and R-NH3+ is an organic ligand bonded to a positively charged ammonium cation. In this study,  $B = Pb^{2+}$ is the inorganic cation, I- is the halide, and R-NH3+ corresponds to one of seven molecules: n-butylammonium (BA), isopentylammonium (iPA), n-hexylammonium (HA), cyclohexanemethylammonium (ChMA), phenylethylammonium (PEA), chloro-phenylethylammonium (Cl-PEA), or fluorophenylethylammonium (F-PEA).[47-52] The seven ligands are selected to encompass a range of steric and electronic properties, such as bulkiness (BA vs. iPA vs. HA), electronegativity (PEA vs. Cl-PEA vs. F-PEA), and molecular flexibility (ChMA vs. PEA); the chemical structures of the ligands and these groupings are displayed in Figure 1b. We note that 2D HOIPs may also form in a Dion-Jacobson (DJ) phase with formula (R-(NH<sub>3</sub>)<sub>2</sub>)<sub>2</sub>BX<sub>4</sub>

wherein a single diammonium cation is used in place of two monoammonium cations in the RP structure.<sup>[53]</sup> This work focuses on RP phase HOIPs because they are more commonly used in passivation layers.

#### 3. Results

#### 3.1. Analysis of Halide Transport Pathways

MD simulations were used to compute the free energy along the in-plane and out-of-plane halide diffusion pathways in seven 2D HOIP systems (Figure 2). Our expectation was that these activation-free energies deduced from simulation could be related to experimental trends in ionic conductivity, such that we could ascertain the impact of different ligands and the relevance of different diffusion pathways. For in-plane (ip) halide migration, we studied two types of diffusion pathways: hopping from an axial site to an equatorial site (Figure 2a,  $ax\rightarrow eq$ ) and hopping from an equatorial site to another adjacent equatorial site (Figure 2a,  $eq\rightarrow eq$ ). For out-of-plane (oop) halide migration, we analyzed paths from one axial site to another axial site across the organic layer and on a different octahedron (Figure 2a,  $ax\rightarrow ax$ ).

Figure 2b compares in-plane and out-of-plane halide activation-free energies across systems (denoted  $\Delta F^{\ddagger(ip)}$  and  $\Delta F^{\ddagger(iop)}$ ). Barriers to in-plane (ax $\rightarrow$ eq, eq $\rightarrow$ eq) diffusion are broadly consistent with prior literature. [42,54] Barriers for eq $\rightarrow$ eq paths are systematically higher than those of ax $\rightarrow$ eq paths, as in computational work for CsPbI<sub>3</sub>. [54] Furthermore, in-plane activation-free energies are comparable to those reported by Akriti et al. [42] (e.g., obtaining 0.52 eV for a quasi-2D HOIP with PEA and 0.37 eV for bulk diffusion in MAPI, also with the MYP force field). There is, however, a stark contrast between in-plane and out-of-plane activation-free energies. Barriers in the out-of-plane direction not only generally exceed those in-plane but also exhibit greater dynamic range (ca. 1.1 eV vs ca. 0.2 eV). These results suggest that out-of-plane transport is both rate-limiting and sensitive to ligand chemistries.

Figure 2c-e highlights potential ligand effects by comparing the free energy pathways for out-of-plane (oop) diffusion within groups with systematic chemical variations. The pathways possess statistically resolvable differences across systems, which yield clear orderings within each group. On the basis of two-point comparisons availed by this ligand set, we find that activationfree energy increases with ligand branching (iPA > BA), length (HA > BA), and stiffness (PEA > ChMA). Meanwhile, activationfree energy decreases with electronegativity (F-PEA < Cl-PEA < PEA); this result is also consistent with recent work comparing 2D perovskite passivation for meta-, ortho-, and para-substitution in various halogenated PEA+ ioidide salts.[25] Ligands with conjugated rings stand out with the highest diffusion barriers, which is also consistent with the trends representing ligand bulk and flexibility. Presuming thermally-activated diffusion, out-of-plane diffusion would be expected to follow the trend: BA > ChMA > iPA > HA > F-PEA > Cl-PEA > PEA.

## 3.2. Comparison to Experimental Results

A limited set of preexisting data and experiments were used to benchmark our computational findings. An important

16146840, 2024, 40, Downloaded from https

com/doi/10.1002/aenm.202401087 by Princeton University, Wiley Online Library on [09/04/2025]. See the Terms

ns) on Wiley Online Library for rules of use; OA articles are governed by the applicable Creative Commons

**SCIENCE NEWS** 

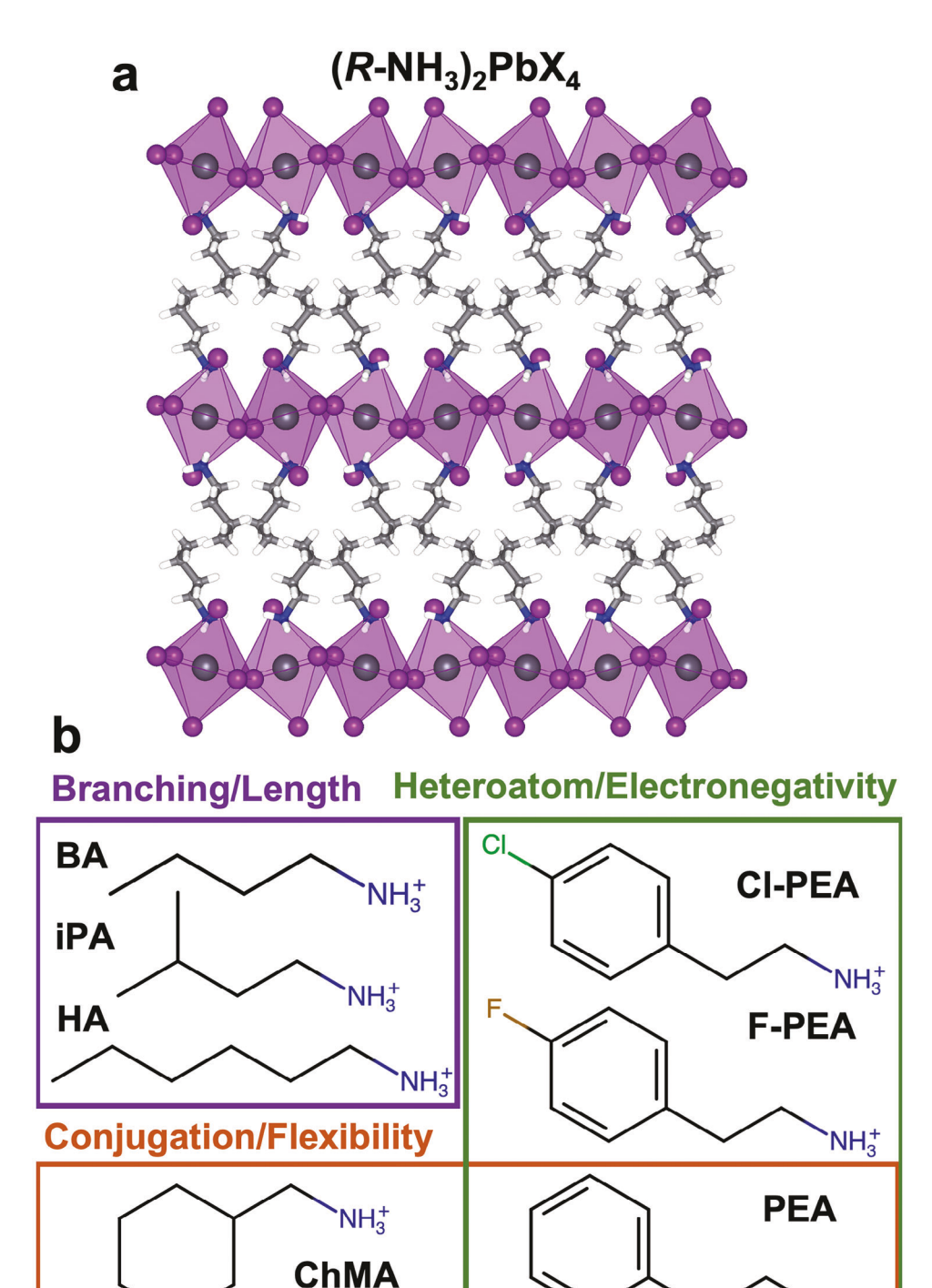


**Figure 1.** Overview of systems. a) Orthographic projection of the 2D hybrid organic—inorganic perovskite structure with n-butylammonium.  $I^-$  is purple, Pb<sup>2+</sup> is dark gray, nitrogen is blue, hydrogen is white, and carbon is light gray. The octahedral geometry of these atoms is illustrated using the purple surfaces; organic ligands are situated between layers of the octahedra. b) The structures of organic ligands studied: n-butylammonium (BA), isopentylammonium (iPA), n-hexylammonium (HA), cyclohexanemethanammonium (ChMA), phenylethylammonium (PEA), chloro-phenylethylammonium (Cl-PEA), and fluoro-phenylethylammonium (F-PEA). Boxes group ligands based on the most direct and intended comparisons. The purple, green, and orange boxes respectively highlight the effects of branching and length, electronegativity, and conjugation and flexibility by systematic variations of the functional chemical groups. Note that PEA is included in both orange and green boxes as it is relevant for both comparisons.

NH<sub>3</sub>

16146840, 2024, 40, Downloaded from https

doi/10.1002/aenm.202401087 by Princeton University, Wiley Online Library on [09/04/2025]. See the Terms

and Conditions (https://onlinelibrary.wiley.

and-conditions) on Wiley Online Library for rules of use; OA articles are governed by the applicable Creative Commons

www.advancedsciencenews.com

www.advenergymat.de

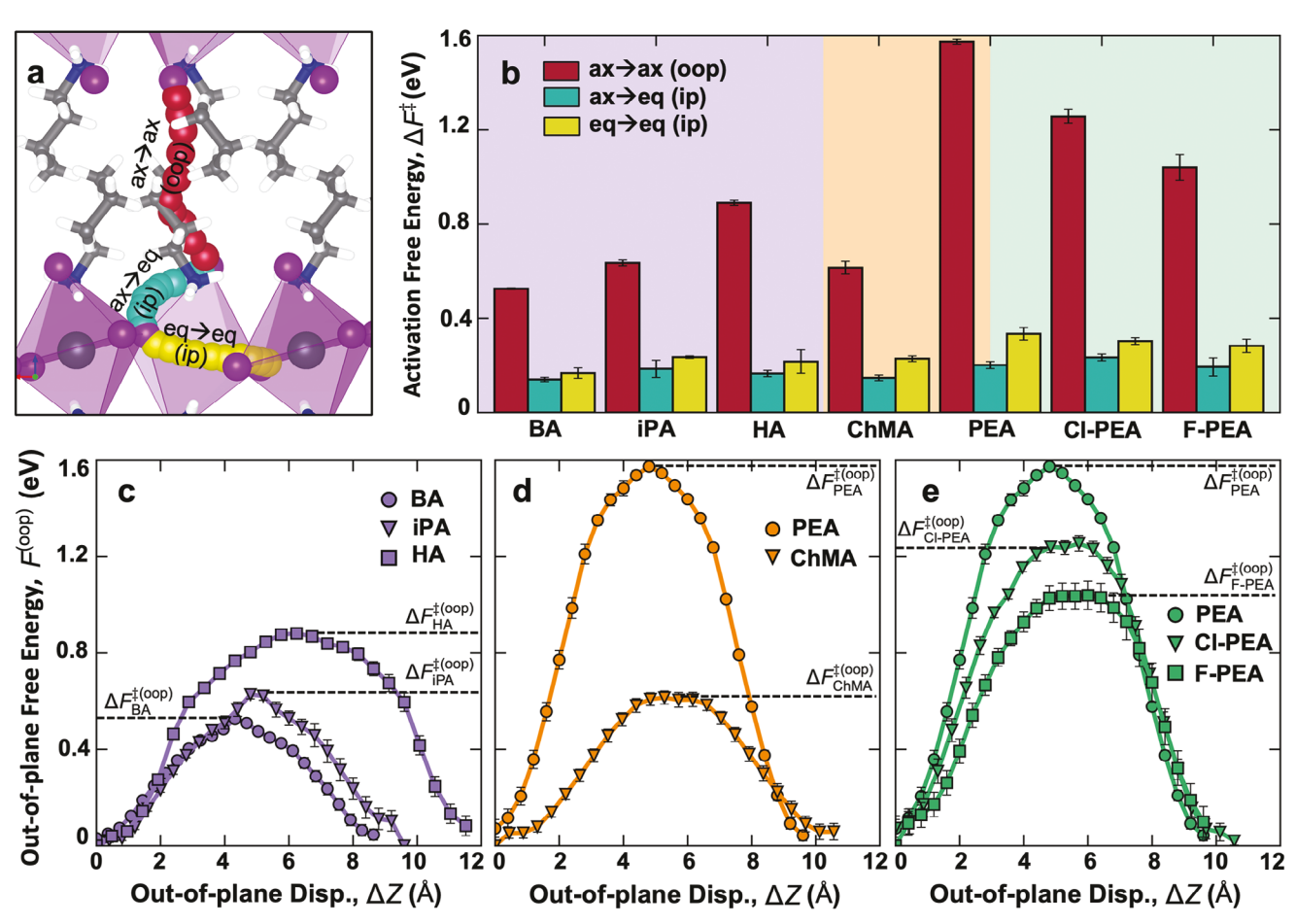


Figure 2. Analysis of vacancy-assisted iodide diffusion pathways. a) Visualization of out-of-plane and in-plane vacancy-assisted iodide diffusion pathways. The red path depicts an axial-to-axial (ax $\rightarrow$ ax) out-of-plane pathway, which necessarily crosses the organic layer, while cyan and yellow paths depict in-plane axial-to-equatorial (ax $\rightarrow$ eq) and equatorial-to-equatorial (eq $\rightarrow$ eq) pathways, respectively. b) Comparison of out-of-plane (oop) and in-plane (ip) activation-free energies  $\Delta F^{\ddagger}$  for different ligands. Background colors correspond to ligand groups delineated in Figure 1b. c–e) Comparison of iodide free energies  $F^{(oop)}$  along out-of-plane diffusion pathways for ligands that principally differ by (c) branching/length, (d) conjugation/flexibility, and (e) electronegativity. The out-of-plane activation-free energy  $\Delta F^{\ddagger(oop)}$  is labeled for each system. Error bars represent standard errors computed across four different transport paths.

factor to consider is whether the simulated crystal structures accurately reflect the ones observed experimentally. Overall, we find a strong correlation between the simulated and experimental crystal structures, with average deviations in parameters being 3% or less (Section SB, Supporting Information). In addition, out-of-plane activation-free energies were extracted for systems with iPA, PEA, and Cl-PEA; unfortunately, characterization of other systems failed due to issues with film stability at elevated temperatures and device construction (Section SG, Supporting Information). Figure 3 depicts consistency in the diffusion trends predicted by simulations and determined by experiment. In the figure, the activation- free energies are normalized by the value for iPA, as simulations exhibited systematically higher values relative to those extracted experimentally. For example, the activation-free energy for PEA is  $1.57 \pm 0.01$  eV compared to  $0.70 \pm 0.10$  eV for simulation and experiment, respectively.

We suspect that the systematic differences arise due to experimental challenges in isolating halide contributions. Specif-

ically, experimental measurements were conducted under a light source, which increases ionic and electronic conduction in HOIPs by up to two orders of magnitude. [55,56] By contrast, the MD results correspond to dark conditions and reflect only contributions from the iodide; attempted experiments in dark conditions did not register sufficient conductivity to be probed by impedance spectroscopy. Although there may also be some differences in activation-free energies between light and dark conditions, this is not expected to remarkably impact the relative ordering amongst ligands. Some discrepancies between simulation and experiment could also be due to inaccuracies in the employed force field, but such issues would likely manifest similarly across the different systems given the consistent parameterization procedure. Additionally, the existence of grain boundaries in thin films, which have previously been shown to exhibit faster ionic conductivity than the bulk,[57] could contribute to the discrepancy between experimental and calculated values. Therefore, despite the differences in magnitude, the experiments at least qualitatively validate the simulations, and both sets

16146840, 2024, 40, Downloaded from https://advan

onlinelibrary.wiley.com/doi/10.1002/acnm.202401087 by Princeton University, Wiley Online Library on [09/04/2025]. See the Terms

ns) on Wiley Online Library for rules of use; OA articles are governed by the applicable Creative Commons

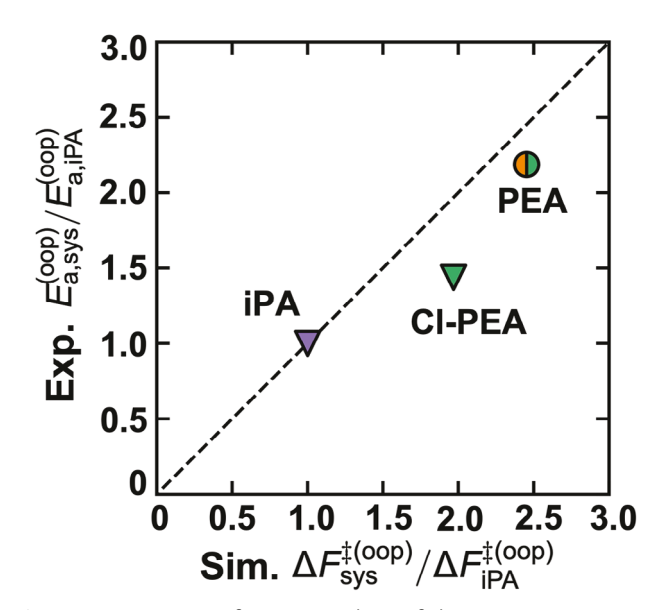


**Figure 3.** Comparison of experimental out-of-plane activation energies,  $E_a^{(\text{oop})}$ , with simulated out-of-plane activation-free energies,  $\Delta F^{\ddagger(\text{oop})}$ . Values are scaled by the iPA out-of-plane activation energy and activation-free energy. The colors and symbols are consistent with those in Figures 1 and 2. The dashed line is a guide to the eye.

of results suggest similar ligand effects on out-of-plane halide diffusion.

#### 3.3. Role of Ligand Length and Flexibility

To better understand how ligand chemistry impacts halide transport, we examined if simple molecular descriptors correlate with activation-free energies (Figure 4). Figure 4a,b conveys that certain structural features of the ligands, such as the molecular flexibility factor, [58] f, and the end-to-end length, L, can directionally predict diffusion trends. Apart from their simplicity, the rationale for considering f is its possible correlation to structural reorganization events, while L may correlate with the complexity of required structural reorganizations. Barriers generally increase with decreasing ligand flexibility. This is demonstrated in Figure 4a by contrasting a group with high flexibility (e.g., BA and iPA) compared to one with lesser flexibility (e.g., PEA and Cl-PEA). This is consistent with the idea that flexible ligands create a "soft" lattice that can facilitate anion diffusivity.[59] The effect of flexibility on the free energy also partially explains the large activation free energies for PEA, Cl-PEA, and F-PEA, as the  $\pi$ -conjugation results in large steric constraints on diffusion pathways.

Flexibility alone does not explain the data, however. For example, the ChMA system possesses a relatively low activation free energy (0.61  $\pm$  0.04 eV), despite being amongst the most rigid (low f) ligands. Examining Figure 4b, we observe that the activation free energy can strongly correlate with ligand length. For example, the activation free energy of HA exceeds that of BA and iPA systems, which both possess backbones that are shorter by two methyl groups. Meanwhile, ChMA is relatively rigid but also amongst the shortest ligands by end-to-end length, thus explaining its low activation free energy. There may also be minor trends

related to branching that likely operate on similar principles as end-to-end length. In particular, iPA has a slightly larger activation free energy than BA despite registering a higher flexibility factor. The effect of bulkiness on the activation free energy can be observed quantitatively between ligands of similar end-to-end length (Section SM, Supporting Information).

Therefore, we suppose that more rigid, longer, and bulkier ligands tend to inhibit out-of-plane halide diffusion by imposing steric constraints on diffusion pathways. It is notable, however, that PEA is neither the most rigid nor the longest nor the bulkiest ligand, yet it exhibits the largest activation free energy. We defer the explanation of this result to Section 3.4.

To gain further insight into the steric effects imposed by ligands, we compare the structural order of the ligands using radial distribution functions (RDFs) g(r) (Figure 5). We select the N-N and I-N RDFs because 'N' is a distinctive atom across all

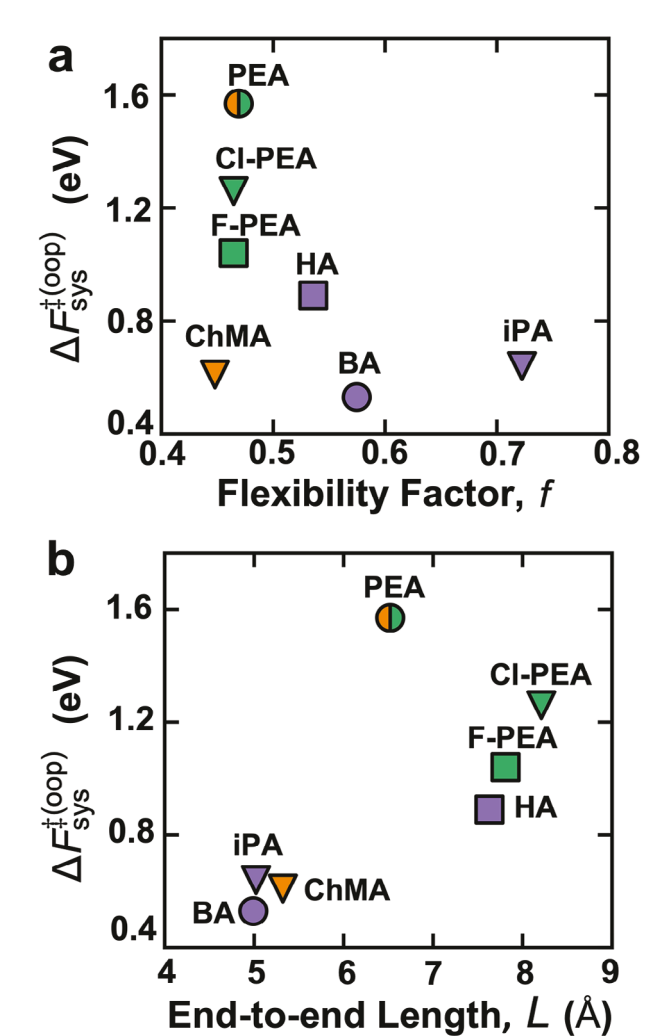


**Figure 4.** Correlation of out-of-plane iodine vacancy activation free energy with ligand a) flexibility f and b) end-to-end length L. The flexibility factor f is extracted from DataWarrior[ $^{58}$ ] and is a function of a molecule's number of rotatable bonds, torsion data, and geometry. The color(s) of each point correlates with the ligand effect from Figure 1b, and the shape corresponds to different species within each ligand group (from Figure  $^{2}$ C-e).

eed on inicibary. wiley, com/doi/10.1002/amm.202401087 by Princeton University, Wiley Online Library on [09/04/2025]. See the Terms and Conditions (https://onlinelibrary.wiley.com/terms-and-conditions) on Wiley Online Library for rules of use; OA articles are governed by the applicable Creative Commons

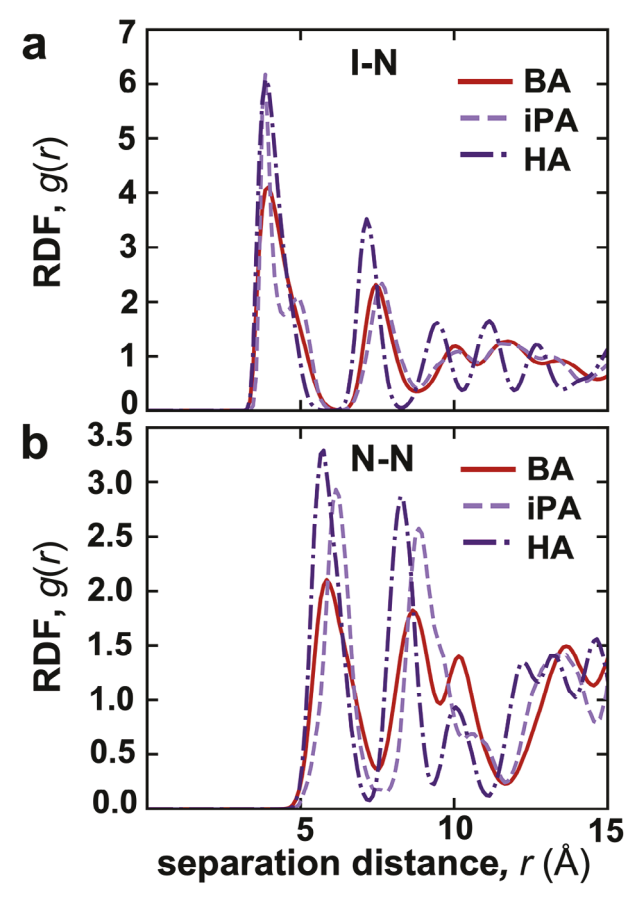


**Figure 5.** Radial distribution functions g(r) between a) I-N and b) N-N for BA, iPA, and HA systems. The g(r) functions are calculated from 200 configurations taken at 1 ps intervals.

the ligands, while 'I' borders the organic layer. Thus, the N-N RDF reveals structure within the organic layer, and the N-I RDF elucidates the ordering of cation ligands at the boundary between the organic and inorganic layers. A full analysis of the RDFs based on multiple Gaussian fits (including heights, positions, widths, and areas) is reported in Section SO (Supporting Information). Our analysis for HA, iPA, and BA of the I-N (Figure 5a) and N-N (Figure 5b) RDFs shows that the presence of narrower and more prominent peaks in the RDF correlates with higher activation-free energies. Both RDFs for HA and iPA exhibit peaks with greater prominence (i.e., taller) and smaller widths than for BA, especially at shorter distances (<8 Å). Moreover, the RDFs for HA have more prominent and narrower peaks than the iPA RDFs, with the I-N RDF being notably more structured at longer distances (> 9 Å). For example, the HA peaks > 9 Å have smaller combined areas than the iPA and BA peaks > 9 Å, despite their heights being larger. The implication of narrower and more prominent peaks at shorter distances (denoted in Figure 5a) for I-N and N-N is that the relative positions of the I and N are more confined or restricted in the vicinity of PbI<sub>2</sub> octahedra. At longer distances, the peaks generally reflect less thermal disorder and thereby enhance structural correlation between the organic and inorganic layers. The increased structural order implies fewer low-free-energy pathways for an ion to traverse an organic layer. In the future, it may be interesting to ascertain whether the trends in enhanced ordering are observed via scattering experiments resolved at high wave vectors ( $q > 30 \text{ Å}^{-1}$ ).

#### 3.4. Role of Ligand Charge Distribution

The trend amongst PEA, Cl-PEA, and F-PEA systems mostly defies the logic espoused in prior sections. Flexibility is not an effective discriminant in this group, and both Cl-PEA and F-PEA are longer than PEA, which has the highest activation-free energy. We find that a combination of factors relating to the structure and electrostatics of the organic layer explain these results (Figure 6). First, comparing RDFs (Figure 6a) reveals that PEA is somewhat more ordered than Cl-PEA and F-PEA, particularly at longer distances, which falls in line with prior arguments about restricting diffusion pathways; however, Cl-PEA and F-PEA are largely similar. Differences between these systems become apparent in the average electrostatic potential  $\phi$  experienced by the migrating iodine atom as it traverses the organic layer (Figure 6b). For PEA, φ is slightly negative, while it is primarily positive for the Cl-PEA and F-PEA systems. Because iodide is negatively charged, a positive  $\phi$  implies attractive forces and a negative  $\phi$  implies repulsive forces. The first-order implication is that the Coulombic repulsion from the organic layer of PEA also enhances the activationfree energy. Interestingly, the electrostatic potential of the F-PEA system is more variable than that of Cl-PEA and characterized by several notable minima. This is further illustrated in Figure 6c, which compares standard deviations of electrostatic potential  $\sigma_{\phi}$ experienced by the diffusing iodide. Only F-PEA exhibits oscillating electrostatic fluctuations along the iodine pathway, suggesting greater spatial charge heterogeneity and varied Coulombic forces within the organic layer. Notably, this effect is not obviously reflected in Figure 5, which mainly captures edge interactions of the organic layer. Thus, the observed energy barrier trend (PEA > Cl-PEA > F-PEA) arises from a charge-repulsive migration pathway in PEA and increased spatial charge heterogeneity in F-PEA, which reflects electrostatic structural disorder within the organic layer.

To further understand the ramifications of charge heterogeneity, Figure 6d overlays the 2D charge density of the organic layer (blue-gray-red color map) along with a projection of two example diffusion paths for an iodide (yellow and green markers). The corresponding molecular configurations are presented in Figure 6e. These density projections and corresponding molecular configurations emphasize how the organic layer of PEA is unlike the structures of Cl-PEA and F-PEA. Interactions between bifunctional ligands (such as Cl-PEA and F-PEA) in the organic layer have previously been shown to modify the bonding characteristics of the ammonium terminus. [60] In PEA, the positively charged ammonia groups alternate in the b direction with the negatively charged iodine of the PbI<sub>2</sub> octahedra. However, in Cl-PEA and F-PEA, the ammonia groups align with the PbI<sub>2</sub> octahedra in the a direction (pointing into the page). Thus, a diffusing iodide experiences fundamentally distinct diffusion pathways between PEA and the ostensibly analogous F-PEA and Cl-PEA. In particular, iodide traversing PEA mostly navigates neutral to repulsive regions whereas iodide in F-PEA or Cl-PEA can travel alongside two organic ligands in the a direction, which allows

16146840, 2024, 40, Downloaded from https

com/doi/10.1002/aenm.202401087 by Princeton University, Wiley Online Library on [09/04/2025]. See the Terms

nditions) on Wiley Online Library for rules of use; OA articles are governed by the applicable Creative Common

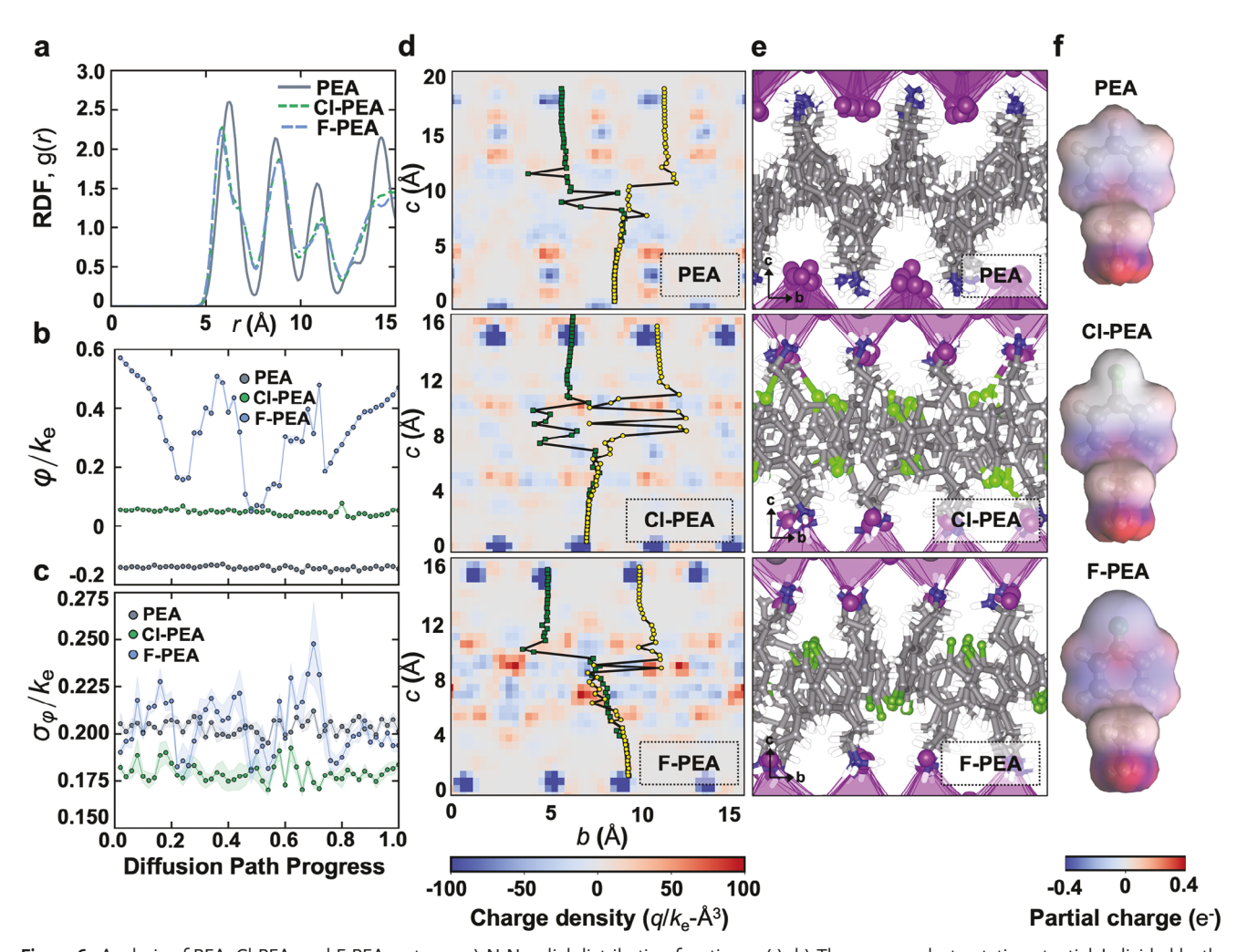


**Figure 6.** Analysis of PEA, Cl-PEA, and F-PEA systems. a) N-N radial distribution functions g(r). b) The average electrostatic potential  $\phi$  divided by the Coulomb constant  $k_e$  along iodide diffusion pathways determined from umbrella sampling. c) The standard deviation of the electrostatic potential  $\sigma_{\phi}$  along the same diffusion pathways as in (b). In (b),(c) the shaded regions represent standard errors (Section SK, Supporting Information); additional checks for statistical significance of the data is provided in the Supplemental Information, Section L. d) The charge density of the organic layer averaged across the *a*-axis for PEAPI, Cl-PEAPI, and F-PEAPI. Two diffusion paths are indicated by the green and yellow markers, with each marker representing the time-averaged position of the migrating iodine atom projected onto the *b-c* plane. The charge density was computed at a grid density of 27 Å<sup>-3</sup> with a 10 Å cutoff using the partial charges from the MYP force field and those determined as described in the Methods and reported in Tables S10–S12 (Supporting Information). e) Representative configurations in the plane of the charge density plots depicted in (d). The images reflect an orthographic projection onto the *c* vs. *b* plane, thereby simultaneously depicting many layers in the *a* direction. f) The partial charge distribution on the individual ligands determined as described in the Experimental Section.

for more attractive electrostatic potentials throughout its trajectory. Interestingly, the electrostatic characteristics and resulting behavior for HA are functionally more similar to Cl-PEA and F-PEA than to PEA, which may contribute to the activation free energy of PEA being greater than HA (Section SN, Supporting Information).

The relative ordering of systems is informed by considering differences in molecular polarizability. By comparison to Cl-PEA, the interior of F-PEA has "hot spots" with heightened positive charge density, which present more favorable environments for the iodide. These hot spots (or lack thereof) are attributed to the disparity in charge distribution over the ligands (Figure 6f). Because F-PEA is more strongly polarized, as might be expected from the stronger electronegativity of fluorine over chlorine,

this generates multiple regions of partial positive and negative charge. Correlations of molecular dipoles with passivation efficiency have been similarly noted to explain the relative performance of placing halogen substituents in meta, ortho, or para positions of phenyl rings. [25] Returning to Figure 6d, the prevalence of these regions allows for shorter "hops" to positive regions during the diffusion pathway compared to Cl-PEA, which sustains greater displacements in the c direction. Although PEA exhibits a similar charge landscape to Cl-PEA, its eclipsed ligands confine the iodide to paths of lower steric resistance, which do not comprise the energetically-favored route alongside two ligands. In summary, the eclipsed PEA system has the highest activation free energy due to its enhanced order and nominally repulsive interior, followed by the staggered Cl-PEA system, followed by

**ADVANCED** SCIENCE NEWS

www.advancedsciencenews.com

ADVANCED ENERGY MATERIALS

www.advenergymat.de

the staggered and more strongly charge-heterogeneous F-PEA system.

## 4. Conclusion

We performed a systematic study of seven distinct 2D HOIP systems to understand the consequences of ligand chemistry for mitigating ion transport in perovskite solar cells. Molecular dynamics simulations were used to first establish that activation free energies for out-of-plane halide diffusion, which has been nascently studied, generally exceed those for in-plane transport, and such free energies are sensitive to ligand chemistry. Moreover, trends in activation free energies for out-of-plane diffusion agreed well between simulation and experiment, although further study is necessary to concretely assess systematic differences. By analyzing the simulations, we then formulated a series of design principles for optimizing ligand chemistry to mitigate out-of-plane halide diffusion in HOIPs. Explanation of all trends requires consideration of both structural and electrostatic effects. Most understanding can be framed through a simple argument of whether ligand effects result in more order or less order within the organic layer, with enhanced order tending to restrict viable diffusion pathways. From a structural standpoint, activation free energies for ion diffusion tend to increase as ligands become bulkier, more rigid, and lengthier. From an electrostatic standpoint, electrostatic potential and heterogeneity of charge distribution over the organic layer can explain most results, although such effects may be harder to anticipate a priori based on ligand chemistry alone. Specifically, lesser polarized ligands generate less favorable free-energy landscapes or more restrictive environments for diffusion pathways, which challenges diffusion. Conversely, more polarized ligands generate more diffusion "hotspots" - positively-charged regions where iodine atoms prefer to hop - thereby minimizing the hop distance and lowering the barrier to diffusion. The robustness of identified trends would benefit from more expansive examination beyond the ligands presented here; such future work could also elucidate the relative importance of potentially competing effects. In addition, the analysis and results presented are strictly limited to iodide as the diffusing species. Although trends are expected to be broadly transferable to different anions (e.g., chloride or bromide), some ligand effects, particularly those depending on structural reorganization, may become less pronounced with smaller diffusing ionic species, while those that depend more on electrostatic effects may be more similar. Similar trends as seen here may also be anticipated in DJ HOIPs, although this requires future investigation as diammonium ligands may exhibit reduced flexibility due to interactions with the inorganic lead iodide octahedral framework at both ends of the ligand. Overall, this work provides new insights into the nature of halide diffusion in 2D HOIPs and offers guidelines that may be useful for engineering passivation materials for perovskite solar cells.

#### 5. Experimental Section

General Simulation Procedures: All MD simulations were performed with LAMMPS using a 1 fs integration time step and periodic bound-

ary conditions.<sup>[61,62]</sup> Interaction parameters were taken from the classical MYP force field developed for 3D MAPbI<sub>3</sub>. [41] The force field was further adapted for the 2D systems following the approach employed by Fridriksson et al. wherein formal charges of +2 and -1 were assigned to the Pb and I atoms, and a +1 charge was distributed over the organic cation. [63] This approach was adopted to increase the transferability of the force field. Partial charges were computed using the following protocol. First, the ligands were built in Avogadro. [64] Next, they underwent initial geometry optimization using the Universal Force Field (UFF)<sup>[65]</sup> followed by optimization at the density functional theory (DFT) level using the BP86 functional, [66,67] a double-zeta basis, [68] the RI-] approximation, [69] and DFT-D3 dispersion correction.<sup>[70,71]</sup> After geometry optimization, partial charges were fit to the electrostatic potential from a DFT calculation using B3LYP functionals and the correlation consistent polarized valence quadruple zeta basis sets (ccpVQZ) using the CHELPG (CHarges from ELectrostatic Potentials using a Grid-based method) approach.[72] DFT calculations were performed using ORCA.[73] The final partial charges were determined by averaging over symmetric atoms and symmetric configurations. All charges and interaction parameters for the seven systems are reported in the Supporting Information. Long-range electrostatics were modeled using the particle-particle-mesh algorithm; short-ranged Lennard-Jones, Buckingham, and Coulombic interactions were truncated at 10 Å.

System Preparation and Simulation: The initial configurations for the seven systems were taken from experimental crystal structure unit cells. [47-52] These cells were then replicated into 4  $\times$  4  $\times$  4 or 4  $\times$  4  $\times$  2 supercells in the three lattice directions a, b, c to construct systems with four layers of lead-iodide. Overlapping atoms were deleted and bonds were connected across the periodic boundaries. The systems were then equilibrated at 300 K in several steps. First, the systems underwent initial relaxation by simulating for 0.5 ns with maximum positional displacements restricted to be within 0.1 Å for any atom for each timestep. Second, systems were simulated under constant temperature and constant zero-stress (N $\sigma$ T) conditions for 10 ns. Third, the volume of the final 2 ns was averaged, and constant temperature, constant volume (NVT) simulations were performed at the averaged volume for 3 ns. Simulations were then run for 2 ns to produce data for analysis and initial reference configurations for free energy calculations.

Free Energy Analysis of Diffusion: The free energy pathway for iodide diffusion was considered by first identifying an initial location A on the lattice and a second vacant position B, which was constructed by removing an iodine from a previously generated reference configuration. After A and B were defined, steered molecular dynamics (SMD)[74] was used to identify an initial pathway for umbrella sampling. [75] From the reference configuration with the B vacancy, a moving spring with spring constant K =  $5000 \frac{kcal}{mol-\mathring{A}^2}$  and pulling velocity  $\nu = -0.000013 \frac{\mathring{A}}{fs}$  was attached between B and A. All atoms besides A were held constant during SMD. For out-of-plane calculations, after the initial pathway was identified, the reaction coordinate Z was split into 50 "windows" from  $Z_A$  to  $Z_B$  with equal spacing. The initial configurations of the diffusing halide A for each  $Z_i$  were extracted from the SMD trajectory in a forward search for each Z-value. For in-plane calculations, the reaction coordinate was set to be the migration distance, and a forward search was performed for the distance from the A atom; 50 windows were also used in these calculations.

For each window, configurations first underwent initial structural relaxation by simulating the system for 0.1 ns with maximum displacements limited to 0.1 Å. This was followed by 2 ns of simulation under NVT conditions. The position of the diffusing halide ion was restrained to a target position using a spring constant  $K=50\frac{\text{kcal}}{\text{mol-Å}^2}$ . In the out-of-plane calculations, the restraint was only applied in the Z (out-of-plane) direction, whereas the restraint was applied to all three Cartesian directions for in-plane calculations. To prevent drift in the system, the halide atoms in the lead-iodide layers away from the diffusing A halide were also mildly restrained using a spring constant of  $0.1\frac{\text{kcal}}{\text{mol-Å}^2}$ . After conducting simulations on the separate windows, the overall free

www.advancedsciencenews.com



www.advenergymat.de

energy profile was generated using the weighted histogram analysis method.  $^{[76,77]}$ 

Chemicals and Reagents: Lead iodide (Pbl<sub>2</sub>) was purchased from TCI Chemicals, and dimethyl formamide (DMF), acetone, and isopropyl alcohol (IPA) were purchased Sigma Aldrich. Isopentylammonium iodide (iPAI), phenylethylammonium iodide (PEAI), and chlorophenylethylammonium iodide (Cl-PEAI) were purchased from Greatcell Solar Ltd. Devices were made on prepatterned indium tin oxide (ITO) on glass. Gold with 99.999% purity was deposited through a shadow mask as electrodes.

Device Preparation: A 25 × 17.5 mm glass with a center ITO strip was used as the device substrate. A 30 nm layer of gold was thermally evaporated onto this glass over the ITO strip at a base pressure of 10<sup>-6</sup> torr at a rate of 0.5 Å sec<sup>-1</sup>. Perovskite films(2D) were grown via a spin-coating method. Solutions with 2 M of iPAPI, PEAPI, and Cl-PEAPI were prepared by dissolving the dry perovskite precursor powder (iPAI, PEAI, Cl-PEAI) and PbI2 with 2:1 molar ratio in DMF. The solutions were shaken on a Vortex shaker for roughly 10 min and then filtered for purity. Perovskite solutions were then spun onto the substrates at 5000 rpm for 35 s and annealed for 10 min at 100°C. The spin-coating was done in a nitrogen-filled glovebox. Next, a 50 nm layer of gold was thermally evaporated on top of the film at a rate of 0.5 Å sec<sup>-1</sup> through a shadow mask. The 9 mm<sup>2</sup> area of the out-of-plane devices was defined by the overlap of top and bottom electrodes. A scratch was made on the device to access the bottom gold electrode. Images detailing the procedure are in the Supporting Information.

Planar orientation of 2D perovskite films was verified by XRD measurements conducted on a Bruker D8 Discover diffractometer using Cu K $\alpha$  radiation source ( $\lambda=1.54$  Å). SEM images of the 2D perovskite films were taken using a FEI Verios 460 XHR SEM with 5 keV accelerating voltage and 25 pA beam current.

Conductivity Measurements: To quantify the ionic conductivity in the 2D layered structures, we separated the ionic conductivity from the combined ionic-electronic conductivity by following the procedure described in Kim et al.<sup>[55]</sup>. In particular, ionic conductivity was calculated as the difference between the total conductivity taken from the high-frequency semicircle measured by alternating-current (AC) impedance spectroscopy and the electronic conductivity taken from the steady-state voltage measured by galvanostatic direct-current (DC) polarization. Ionic conductivity as a function of temperature was fit by the Arrhenius equation to extract the activation energy. All measurements were done on a Lake Shore Cryotronics probe station in a nitrogen environment under white light with an intensity of 61 W m<sup>-</sup> to facilitate the generation of charge carriers. A Lakeshore 366 temperature controller was used to heat devices for activation energy measurements. Impedance spectroscopy was measured using a CH Instruments 660C electrochemical workstation. Galvanostatic DC polarization measurements were performed using a Keithley 2400 sourcemeter. Data is provided in the Supporting Information.

### **Supporting Information**

Supporting Information is available from the Wiley Online Library or from the author.

## Acknowledgements

H.Z. and M.A.W. acknowledge support from the "Chemistry in Solution and at Interfaces" (CSI) Center funded by the U.S. Department of Energy through Award No. DE-SC0019394. Simulations and analyses were performed using resources from the Princeton Research Computing at Princeton University, which is a consortium led by the Princeton Institute for Computational Science and Engineering (PICSciE) and the Office of Information Technology's Research Computing. Simulations were performed using resources from the Princeton Research Computing at the Princeton University, which is a consortium led by the Princeton Institute for Computational Science and Engineering (PICSciE) and the Office of Information

Technology's Research Computing. A.B.K. acknowledges support from the National Science Foundation Graduate Research Fellowship Program under Grant No. DGE-2039656. Y.L.L. and A.B.K. acknowledge support from the U.S. Department of Energy's Office of Energy Efficiency and Renewable Energy (EERE) under Solar Energy Technologies Office (SETO) Agreement Number DE-EE0010503. The authors acknowledge the use of the Imaging and Analysis Center (IAC) operated by the Princeton Materials Institute at Princeton University, which is supported in part by the Princeton Center for Complex Materials (PCCM), a National Science Foundation (NSF) Materials Research Science and Engineering Center (MRSEC; DMR-2011750).

#### **Conflict of Interest**

The authors declare no conflict of interest.

# **Data Availability Statement**

The data that support the findings of this study are available in the supplementary material of this article.

### **Keywords**

degradation, halide diffusion, molecular dynamics, organic solar cells, passivation, photovoltaics

Received: March 9, 2024 Revised: July 6, 2024 Published online: July 24, 2024

- [1] T. M. Brenner, D. A. Egger, L. Kronik, G. Hodes, D. Cahen, *Nat. Rev. Mater.* 2016, 1, 1.
- [2] R. Vidal, J.-A. Alberola-Borràs, N. Sánchez-Pantoja, I. Mora-Seró, Adv. Energy Sustainability Res. 2021, 2, 2000088.
- [3] W. Li, Z. Wang, F. Deschler, S. Gao, R. H. Friend, A. K. Cheetham, Nat. Rev. Mater. 2017, 2, 1.
- [4] Z. Xiao, Y. Zhou, H. Hosono, T. Kamiya, N. P. Padture, Chem. Eur. J. 2018, 24, 2305.
- [5] Best Research-Cell Efficiency Chart.
- [6] G. Niu, X. Guo, L. Wang, J. Mater. Chem. A 2015, 3, 8970.
- [7] D. Wang, M. Wright, N. K. Elumalai, A. Uddin, Sol. Energy Mater. Sol. Cells 2016, 147, 255.
- [8] C. A. Aranda, L. Caliò, M. Salado, Crystals 2021, 11, 519.
- [9] X. Zhao, T. Liu, Q. C. Burlingame, T. Liu, R. Holley, G. Cheng, N. Yao, F. Gao, Y.-L. Loo, *Science* 2022, 377, 307.
- [10] D. Meggiolaro, E. Mosconi, F. De Angelis, ACS Energy Lett. 2019, 4, 779.
- [11] L. Bertoluzzi, C. C. Boyd, N. Rolston, J. Xu, R. Prasanna, B. C. O'Regan, M. D. McGehee, Joule 2020, 4, 109.
- [12] J. Carrillo, A. Guerrero, S. Rahimnejad, O. Almora, I. Zarazua, E. Mas-Marza, J. Bisquert, G. Garcia-Belmonte, *Adv. Energy Mater.* **2016**, *6*, 1502246.
- [13] Y. Shao, Z. Xiao, C. Bi, Y. Yuan, J. Huang, Nat. Commun. 2014, 5, 5784.
- [14] H. Zhang, L. Pfeifer, S. M. Zakeeruddin, J. Chu, M. Grätzel, Nat. Rev. Chem. 2023, 7, 632.
- [15] B. Chen, P. N. Rudd, S. Yang, Y. Yuan, J. Huang, Chem. Soc. Rev. 2019, 48, 3842.
- [16] X. Zhou, W. Qi, J. Li, J. Cheng, Y. Li, J. Luo, M. J. Ko, Y. Li, Y. Zhao, X. Zhang, Sol. RRL 2020, 4, 2000308.
- [17] P. Wang, J. Wang, X. Zhang, H. Wang, X. Cui, S. Yuan, H. Lu, L. Tu, Y. Zhan, L. Zheng, J. Mater. Chem. A 2018, 6, 15853.

**ENERGY** www.advancedsciencenews.com www.advenergymat.de

- [18] X. Zheng, B. Chen, J. Dai, Y. Fang, Y. Bai, Y. Lin, H. Wei, X. C. Zeng, J. Huang, Nat. Energy 2017, 2, 1.
- [19] C. C. Stoumpos, D. H. Cao, D. J. Clark, J. Young, J. M. Rondinelli, J. I. Jang, J. T. Hupp, M. G. Kanatzidis, Chem. Mater. 2016, 28, 2852.
- [20] J.-W. Lee, S. Tan, S. I. Seok, Y. Yang, N.-G. Park, Science 2022, 375, eabj1186.
- [21] L. Mao, C. C. Stoumpos, M. G. Kanatzidis, J. Am. Chem. Soc. 2019, 141, 1171.
- [22] A. Caiazzo, R. A. J. Janssen, Adv. Energy Mater. 2022, 12, 2202830.
- [23] Y. Lin, Y. Bai, Y. Fang, Q. Wang, Y. Deng, J. Huang, ACS Energy Lett. 2017. 2. 1571.
- [24] Akriti, E. Shi, S. B. Shiring, J. Yang, C. L. Atencio-Martinez, B. Yuan, X. Hu, Y. Gao, B. P. Finkenauer, A. J. Pistone, Y. Yu, P. Liao, B. M. Savoie, L. Dou, Nat. Nanotechnol. 2021, 16, 584.
- [25] Z. Gozukara Karabag, A. Karabag, U. Gunes, X. Gao, O. A. Syzgantseva, M. A. Syzgantseva, F. Varlioglu Yaylali, N. Shibayama, H. Kanda, A. I. Rafieh, R. C. Turnell-Ritson, P. J. Dyson, S. Yerci, M. K. Nazeeruddin, G. Gunbas, Adv. Energy Mater. 2023, 13, 45.
- [26] U. Gunes, F. V. Yaylali, Z. Gozukara Karabag, X.-X. Gao, O. A. Syzgantseva, A. Karabag, G. B. Yildirim, K. Tsoi, N. Shibayama, H. Kanda, A. I. Rafieh, L. Zhong, A. Züttel, P. J. Dyson, S. Yerci, M. K. Nazeeruddin, G. Gunbas, Cell Rep. Phys. Sci. 2023, 4, 101380.
- [27] P. Delugas, C. Caddeo, A. Filippetti, A. Mattoni, J. Phys. Chem. Lett. 2016, 7, 2356.
- [28] T.-Y. Yang, G. Gregori, N. Pellet, M. Grätzel, J. Maier, Angew. Chem., Int. Ed. 2015, 54, 7905.
- [29] A. Senocrate, I. Moudrakovski, G. Y. Kim, T.-Y. Yang, G. Gregori, M. Grätzel, J. Maier, Angew. Chem., Int. Ed. 2017, 56, 7755.
- [30] Y. Huang, W.-J. Yin, Y. He, J. Phys. Chem. C 2018, 122, 1345.
- [31] C. Eames, J. M. Frost, P. R. F. Barnes, B. C. O'Regan, A. Walsh, M. S. Islam, Nat. Commun. 2015, 6, 7497.
- [32] F. Jiang, J. Pothoof, F. Muckel, R. Giridharagopal, J. Wang, D. S. Ginger, ACS Energy Lett. 2021, 6, 100.
- [33] C. Li, H. Ma, T. Li, J. Dai, M. A. J. Rasel, A. Mattoni, A. Alatas, M. G. Thomas, Z. W. Rouse, A. Shragai, S. P. Baker, B. J. Ramshaw, J. P. Feser, D. B. Mitzi, Z. Tian, Nano Lett. 2021, 21, 3708.
- [34] L. Pedesseau, D. Sapori, B. Traore, R. Robles, H.-H. Fang, M. A. Loi, H. Tsai, W. Nie, I.-C. Blancon, A. Neukirch, S. Tretiak, A. D. Mohite, C. Katan, J. Even, M. Kepenekian, ACS Nano 2016, 10, 9776.
- J. S. Bechtel, A. Van der Ven, Phys. Rev. Mater. 2018, 2, 045401.
- [36] R. A. De Souza, D. Kemp, M. J. Wolf, A. H. H. Ramadan, J. Phys. Chem. Lett. 2022, 13, 11363.
- [37] J. Chen, D. Lee, N.-G. Park, ACS Appl. Mater. Interfaces 2017, 9, 36338.
- [38] C. Kim, T. D. Huan, S. Krishnan, R. Ramprasad, Sci. Data 2017, 4, 170057.
- [39] C. Quarti, E. Mosconi, F. D. Angelis, Phys. Chem. Chem. Phys. 2015, 17, 9394.
- [40] J. Su, Q. Zheng, Y. Shi, J. Zhao, J. Phys. Chem. Lett. 2020, 11, 9032.
- [41] A. Mattoni, A. Filippetti, M. I. Saba, P. Delugas, J. Phys. Chem. C 2015, 119, 17421.
- [42] Akriti, S. Zhang, Z.-Y. Lin, E. Shi, B. P. Finkenauer, Y. Gao, A. J. Pistone, K. Ma, B. M. Savoie, L. Dou, Adv. Mater. 2021, 33, 2105183.
- [43] Akriti, Z.-Y. Lin, J. Y. Park, H. Yang, B. M. Savoie, L. Dou, APL Mater. 2022, 10, 040903.
- [44] Y. Wu, D. Wang, J. Liu, H. Cai, Nanomaterials 2021, 11, 775.
- [45] J. M. Azpiroz, E. Mosconi, J. Bisquert, F. D. Angelis, Energy Environ. Sci. **2015**, *8*, 2118.
- [46] D. J. Kubicki, D. Prochowicz, A. Hofstetter, P. Péchy, S. M. Zakeeruddin, M. Grätzel, L. Emsley, J. Am. Chem. Soc. 2017, 139,

- [47] A. H. Slavney, R. W. Smaha, I. C. Smith, A. Jaffe, D. Umeyama, H. I. Karunadasa, Inorg. Chem. 2017, 56, 46.
- [48] D. B. Straus, N. Iotov, M. R. Gau, Q. Zhao, P. J. Carroll, C. R. Kagan, I. Phys. Chem. Lett. 2019, 10, 1198.
- [49] B. Febriansyah, T. M. Koh, Y. Lekina, N. F. Jamaludin, A. Bruno, R. Ganguly, Z. X. Shen, S. G. Mhaisalkar, J. England, Chem. Mater. 2019,
- [50] Z. Li, M. A. Najeeb, L. Alves, A. Z. Sherman, V. Shekar, P. Cruz Parrilla, I. M. Pendleton, W. Wang, P. W. Nega, M. Zeller, J. Schrier, A. J. Norquist, E. M. Chan, Chem. Mater. 2020, 32, 5650.
- [51] J. M. Hoffman, C. D. Malliakas, S. Sidhik, I. Hadar, R. McClain, A. D. Mohite, M. G. Kanatzidis, Chem. Sci. 2020, 11, 12139.
- [52] D. G. Billing, A. Lemmerer, Acta Crystallogr., Sect. B: Struct. Sci. 2007, 63. 735.
- [53] X. Zhao, T. Liu, Y. Loo, Adv. Mater. 2021, 34, 3.
- [54] M. Pols, J. M. Vicent-Luna, I. Filot, A. C. T. van Duin, S. Tao, J. Phys. Chem. Lett. 2021, 12, 5519.
- [55] G. Y. Kim, A. Senocrate, Y.-R. Wang, D. Moia, J. Maier, Angew. Chem., Int. Ed. 2021, 60, 820.
- [56] G. Y. Kim, A. Senocrate, T.-Y. Yang, G. Gregori, M. Grätzel, J. Maier, Nat. Mater. 2018, 17, 445.
- [57] M. Ghasemi, B. Guo, K. Darabi, T. Wang, K. Wang, C.-W. Huang, B. M. Lefler, L. Taussig, M. Chauhan, G. Baucom, T. Kim, E. D. Gomez, J. M. Atkin, S. Priya, A. Amassian, Nat. Mater. 2023, 22, 329.
- [58] T. Sander, J. Freyss, M. von Korff, C. Rufener, J. Chem. Inf. Model. 2015 55 460
- [59] M. Lai, A. Obliger, D. Lu, C. S. Kley, C. G. Bischak, Q. Kong, T. Lei, L. Dou, N. S. Ginsberg, D. T. Limmer, P. Yang, Proc. Natl. Acad. Sci. USA 2018, 115, 11929.
- [60] X. Zhao, M. L. Ball, A. Kakekhani, T. Liu, A. M. Rappe, Y. L. Loo, Nat. Commun. 2022, 13, 1.
- [61] A. P. Thompson, H. M. Aktulga, R. Berger, D. S. Bolintineanu, W. M. Brown, P. S. Crozier, P. J. in 't Veld, A. Kohlmeyer, S. G. Moore, T. D. Nguyen, R. Shan, M. J. Stevens, J. Tranchida, C. Trott, S. J. Plimpton, Comp. Phys. Comm. 2022, 271, 108171.
- [62] S. Plimpton, J. Comput. Phys. 1995, 117, 1.
- [63] M. B. Fridriksson, S. Maheshwari, F. C. Grozema, J. Phys. Chem. C 2020, 124, 22096.
- [64] M. D. Hanwell, D. E. Curtis, D. C. Lonie, T. Vandermeersch, E. Zurek, G. R. Hutchison, J. Cheminf. 2012, 4, 17.
- [65] A. K. Rappe, C. J. Casewit, K. S. Colwell, W. A. Goddard, W. M. Skiff, J. Am. Chem. Soc. 1992, 114, 10024.
- [66] A. D. Becke, Phys. Rev. A 1988, 38, 3098.
- [67] J. P. Perdew, Phys. Rev. B 1986, 33, 8822.
- [68] F. Weigend, R. Ahlrichs, Phys. Chem. Chem. Phys. 2005, 7, 3297.
- [69] F. Weigend, Phys. Chem. Chem. Phys. 2006, 8, 1057.
- [70] S. Grimme, J. Antony, S. Ehrlich, H. Krieg, J. Chem. Phys. 2010, 132, 154104.
- [71] S. Grimme, S. Ehrlich, L. Goerigk, J. Comput. Chem. 2011, 32, 1456.
- [72] C. M. Breneman, K. B. Wiberg, J. Comput. Chem. 1990, 11, 361.
- [73] F. Neese, F. Wennmohs, U. Becker, C. Riplinger, J. Chem. Phys. 2020, 152, 224108.
- [74] S. Izrailev, S. Stepaniants, B. Isralewitz, D. Kosztin, H. Lu, F. Molnar, W. Wriggers, K. Schulten, in (Eds.: P. Deuflhard, J. Hermans, B. Leimkuhler, A. E. Mark, S. Reich, R. D. Skeel), Computational Molecular Dynamics: Challenges, Methods, Ideas, Springer, Berlin, Heidelberg, ISBN 978-3-642-58360-5, 1999, pp 39-65.
- [75] G. M. Torrie, J. P. Valleau, J. Comput. Phys. 1977, 23, 187.
- [76] S. Kumar, J. M. Rosenberg, D. Bouzida, R. H. Swendsen, P. A. Kollman, J. Comput. Chem. 1992, 13, 1011.
- [77] A. Grossfield, Wham: the weighted histogram analysis method.